https://doi.org/10.5194/egusphere-2026-5431
Preprint. Discussion started: 22 September 2026

Ground ice distribution and degradation rates in the near-shore coastal zone

Craig Warren[1], James Martin[1], Michael Lim[1], Georgia Coote[1], Luke Macpherson[1], Rebecca Lee[2], and Dustin Whalen[2]

[1]School of Engineering, Physics, and Mathematics, Northumbria University, Newcastle upon Tyne, UK
[2]Geological Survey of Canada, Natural Resources Canada, Dartmouth, Canada

Correspondence: Craig Warren (craig.warren@northumbria.ac.uk)

Abstract. Ice-rich permafrost coasts are among the most rapidly changing shorelines on Earth, and their retreat is episodic and highly variable along-shore, which makes planning and management difficult. Massive ground ice within and beneath coastal bluffs is a primary control on that retreat, yet its three-dimensional distribution cannot be assessed from surface observations and is rarely characterised at the resolution coastal protection decisions require. We present a dense three-dimensional Ground Penetrating Radar (GPR) survey, combined with passive seismic Horizontal-to-Vertical Spectral Ratio (HVSR) measurements, photogrammetry, and active layer thickness probing with validation pits, acquired across the beach at Qikiqtarjuak (Tuktoyaktuk Island), Beaufort Sea, Northwest Territories, Canada, over three summer campaigns. The GPR resolves the upper surface of a massive ice body dipping seaward at approximately 1:5, from 0.4 to 2 m below the beach, with along-shore variability resolvable only through dense three-dimensional survey. Repeat survey over a five-year interval yields the first direct measurements of coastal massive ice degradation at this site: a mean of 6 ± 2 cm yr^{-1} along a mid-beach transect, rising to 14 ± 2 cm yr^{-1} in the shallowest ice sampled. The rate decays exponentially with overburden thickness, with a decay length of 40 cm. Read through the thermal damping-depth relation, that length scale implies a surface forcing period of 7–27 days, excluding the diurnal tidal constituents and the annual cycle and pointing instead to fortnightly-scale wetting of the beach by spring tides and storm surge. Rising thawing indices account for the magnitude of the mean rate; the fortnightly signal governs how it varies with depth. The depth-dependence of ground ice loss therefore appears to be set by the frequency with which the surface is wetted, rather than by overburden insulation alone. That control is not fixed: it will shift as open-water seasons lengthen and storm frequency changes, and armouring a beach necessarily alters it. The baseline established here, immediately prior to rock armour installation in March 2025, provides a direct test of that expectation.

1 Introduction

Permafrost degradation in Arctic coastal zones is accelerating under climate change, with consequences that extend well beyond the local landscape. Thawing permafrost releases stored carbon as greenhouse gases, contributing to positive climate feedback mechanisms (Schuur et al., 2015), destabilises coastal bluffs, and threatens the infrastructure and livelihoods of Arctic communities (Irrgang et al., 2019; Ramage et al., 2021). In regions where atmospheric temperatures are rising at up

https://doi.org/10.5194/egusphere-2026-5431
Preprint. Discussion started: 22 September 2026

to four times the global mean rate (Rantanen et al., 2022), these processes are compounding rapidly. A particularly important and poorly understood component of this system is ground ice: excess ice within the permafrost column whose distribution, volume, and rate of change exert strong control over how and where the landscape responds to warming (Lim et al., 2020).

Ice-rich permafrost typically comprises three elements: a seasonally thawing "active layer" (generally <1 m deep), perennially frozen permafrost beneath (which may extend several hundred metres), and volumes of excess ice known as ground ice or massive ice (Lewkowicz et al., 2025). Ground ice forms through a variety of mechanisms — including ice segregation, intrusive ice, and wedge ice — and its spatial distribution is notoriously difficult to predict. Volumetric ice content can vary from near zero to nearly pure ice over distances of just a few metres with little discernible change at the ground surface (Mackay, 1972). This unpredictability has significant practical consequences: where massive ice underlies coastal bluffs or near-shore tundra, thermomechanical erosion can be rapid and non-linear, as ice exposure accelerates melting and undercutting in a self-reinforcing cycle (Dallimore et al., 1996). Understanding the three-dimensional distribution of ground ice at a site scale is therefore a critical step towards quantifying coastal vulnerability and informing protection strategies.

Tuktoyaktuk is a hamlet of approximately 900 people situated near the Mackenzie River delta in the Inuvialuit Settlement Region (ISR), Northwest Territories (NWT), Canada. It is among the most climate-vulnerable communities in the Arctic, characterised by extensive ground ice volumes, increasing storm surge frequency, and rapid coastal change (Lim et al., 2020). The geological history of the area is complex, shaped by successive glacial, marine, lacustrine, and permafrost processes (Couture and Pollard, 2007). Since the onset of Arctic amplification, air temperatures in the region have risen sharply: the mean annual air temperature at Tuktoyaktuk rose from -9.2 °C over 1996–2006 to -7.8 °C over 2015–2024 (Environment and Climate Change Canada station 2203914), several times the global mean rate over the same period (Hansen et al., 2010; Lenssen et al., 2019). Qikiqtarjuak (Tuktoyaktuk Island), situated to the north-east of the hamlet, is a natural barrier island that provides critical protection to the community and its harbour from the Beaufort Sea and Arctic Ocean. The island is dominated by massive ice — most likely a combination of segregated ice and overlying ice wedges (Whalen et al., 2022) — overlaid by Quaternary-aged clayey-silts and sand, with an active layer of <1 m and predominantly lowland tundra at the surface (Lapham et al., 2020).

Coastal erosion of the island is severe and accelerating. Retreat rates on the north-west facing shore, exposed to the open ocean, have increased from approximately 1.5–2 m yr^{-1} to around 5 m yr^{-1} in recent years (Whalen et al., 2022), while the more sheltered south-east shore erodes at approximately 0.48 m yr^{-1} (Whalen et al., 2022). At its narrowest point the island measured only 36 m across in 2022, and predictions based on current trends suggest breach within the next 5–20 years (Lim et al., 2020; Whalen et al., 2022). Such a breach would expose the hamlet and harbour to direct wave attack from dominant north and north-westerly storm tracks (Manson and Solomon, 2007; Kokelj et al., 2012), with severe socioeconomic consequences for both the local community and wider regional supply and transportation networks. In March 2025, rock armour was installed along the north-west facing beach as an emergency coastal protection measure. However, the effects of this intervention on the thermal and mechanical behaviour of the underlying ground ice remain unknown, and there is currently no high-resolution three-dimensional characterisation of the ground ice distribution against which future change can be assessed.

https://doi.org/10.5194/egusphere-2026-5431
Preprint. Discussion started: 22 September 2026

The presence of subsea permafrost offshore of the island further complicates the picture. Relic terrestrial permafrost, frozen at the Last Glacial Maximum, has been progressively inundated by seawater and is now degrading beneath the seafloor (Overduin et al., 2019). The geometry of this subsea permafrost reflects the erosion history of each shoreline. The ice-bearing permafrost table (IBPT) — the depth at which pore ice first occurs, and hence the upper surface of the frozen sediment column — is relatively shallow and gently dipping on the rapidly eroding northern side, whereas on the more slowly eroding southern side it dips more steeply, which Erkens et al. (2025) attribute to longer inundation times. Understanding how terrestrial ground ice and subsea permafrost interact in this transitional near-shore zone is key to linking marine and terrestrial processes and to interpreting the full extent of coastal instability at the site.

Non-destructive geophysical methods offer a practical means of imaging permafrost and ground ice in Arctic environments. Ground penetrating radar (GPR) has been applied to permafrost investigations since the 1970s, with early work at Tuktoyaktuk demonstrating detection of frozen/unfrozen interfaces to depths of approximately 5 m (Annan and Davis, 1976; Davis et al., 1976), and subsequent studies achieving penetration of up to 50 m in partially frozen Alaskan sands (Arcone et al., 1998). GPR has since been used to investigate active layer soil moisture (Moorman et al., 2003; Gacitúa et al., 2011), seasonal freeze-thaw dynamics (Shen et al., 2018), temporal change at field scales (Brosten et al., 2006; Sudakova et al., 2021), and the internal structure of massive ice bodies, including the pingos of the Pingo Canadian Landmark adjacent to Tuktoyaktuk (Bradford et al., 2024). Where radar alone is limited, pairing GPR with a second geophysical method can extend the characterisation: capacitive coupled resistivity has been used alongside GPR to map ground ice elsewhere in the Northwest Territories (De Pascale et al., 2008). Passive seismic methods offer a further complementary means of characterising the subsurface, being sensitive to mechanical property contrasts that may not produce strong electromagnetic reflections, and requiring no active source (Overduin et al., 2015). In marine and nearshore settings, electrical resistivity tomography (ERT) has also proven effective for detecting subsea permafrost and estimating IBPT depths (Overduin et al., 2012; Angelopoulos et al., 2019; Erkens et al., 2025).

Three-dimensional GPR has been applied to ground ice in several settings: to ice-wedge networks in upland tundra at Barrow, Alaska (Munroe et al., 2007), to coexisting ice and soil wedges in maritime periglacial terrain at Kapp Linné, Svalbard (Watanabe et al., 2013), to relict sediment-filled wedge networks at mid-latitudes (Doolittle and Nelson, 2009), to ice complex deposits on Bol'shoy Lyakhovsky Island, where two lithological interfaces were traced below 20 m depth to construct a three-dimensional cryostratigraphic model (Schennen et al., 2016), and to polygonal wedge structures on the Siberian Arctic coast (Edemsky et al., 2024). Seasonal repeat surveys over ice complex deposits have additionally been used to assess how GPR performance varies with ground conditions (Schennen et al., 2022). These studies image subsurface structure at a single epoch, or repeat acquisition in order to characterise the method rather than to measure change in the ground itself. To our knowledge, dense three-dimensional GPR has not been applied to massive ice beneath an actively eroding, periodically inundated beach, nor repeated across years to resolve rates of ground ice degradation, nor combined with passive seismic measurements to extend characterisation beyond the depth at which the radar signal is lost in saturated sediment.

In this paper, we present results from a dense three-dimensional GPR survey, combined with passive seismic measurements and active layer thickness (ALT) probing, acquired across the near-shore coastal zone of Qikiqtarjuak (Tuktoyaktuk Island). Together, these data allow us to construct a three-dimensional image of the ground ice body, characterise its spatial variability

https://doi.org/10.5194/egusphere-2026-5431
Preprint. Discussion started: 22 September 2026

and depth profile, and relate its geometry to the subsea permafrost mapped offshore of the north-west shore. Contrasting erosion rates and subsea permafrost geometry between the island's two shorelines are drawn from published work (Whalen et al., 2022; Lim et al., 2020; Erkens et al., 2025); the geophysical surveys reported here are confined to the north-west coast. This characterisation provides a baseline for evaluating the effects of recent rock armour installation and for informing future coastal protection design. In Section 2 we describe the study site, field conditions, and methods applied, before presenting and discussing results in Section 3 and drawing conclusions in Section 4.

2 Location and Methods

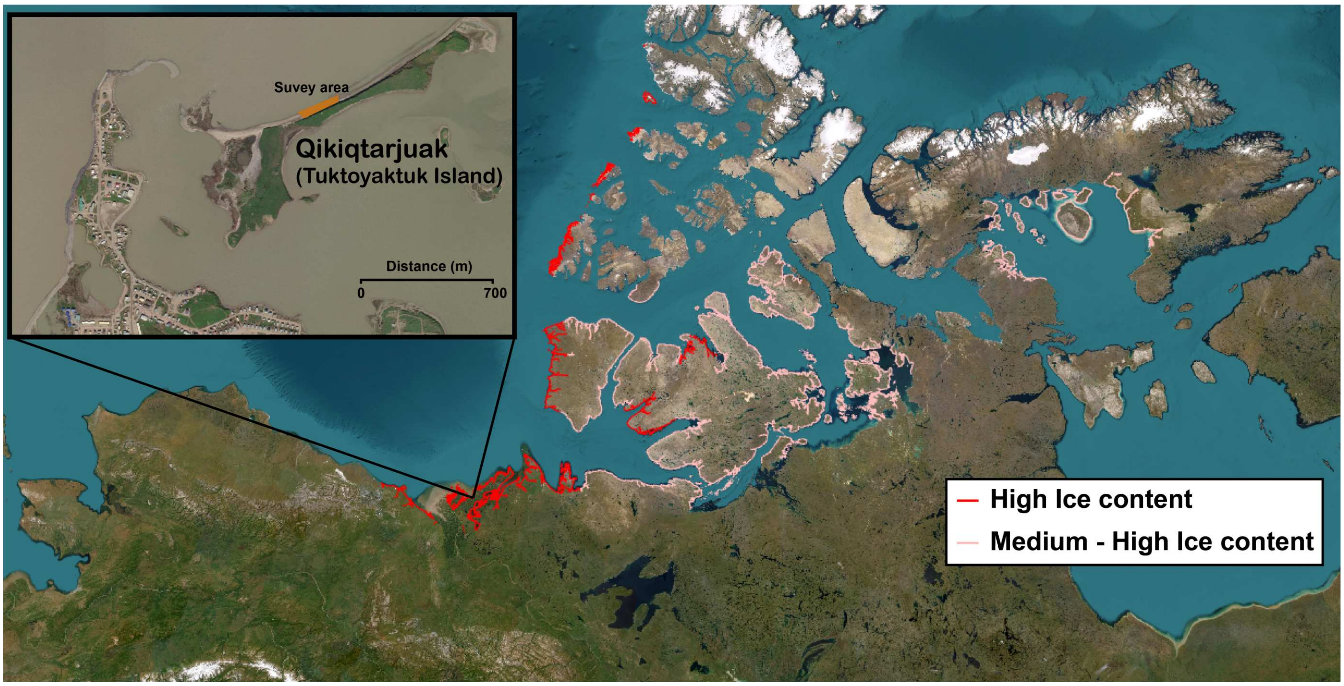

Figure 1. Distribution of high (red) and medium–high (pink) ice content permafrost across the Tuktoyaktuk Peninsula, Northwest Territories, Canada. The inset shows Qikiqtarjuak (Tuktoyaktuk Island) and the hamlet of Tuktoyaktuk, with the harbour basin between them. Basemap imagery: Esri, Maxar, Earthstar Geographics.

Qikiqtarjuak (Tuktoyaktuk Island) lies in the Beaufort Sea immediately north-east of the hamlet of Tuktoyaktuk (Fig. 1). The north-west coast of the island is exposed directly to the open ocean and is characterised by a 1–6 m wide beach backed by cliffs that reach approximately 9 m in height at the survey site, where massive ice is frequently exposed following storm events (Fig. 2). Water was observed to reach the cliff toe during storms, and time-lapse imagery confirms inundation across the full beach width, so the entire surface on which the geophysical measurements were made is subject to periodic wetting. Geophysical measurements were made on this beach, between the base of the cliff and the sea at low tide, over three summer

https://doi.org/10.5194/egusphere-2026-5431
Preprint. Discussion started: 22 September 2026

field campaigns in 2018, 2023, and 2024. The tidal range at Tuktoyaktuk is approximately 1 m, classifying it as micro-tidal, and surveys were timed around low tide to maximise the available survey area (Government of Canada, 2025). In March 2025, rock armour was installed along the north-west facing beach following the survey campaigns reported here; the pre-installation surveys therefore provide a baseline characterisation of the ground ice geometry prior to any modification of the thermal and hydrological regime by the rock armour.

To characterise the electrical properties of the near-surface materials, which govern GPR signal attenuation and penetration depth, conductivity was measured in the field with a YSI ProDSS multiparameter instrument. The probe was immersed in seawater (1 S/m) and in samples of partially saturated (0.0045 S/m) and fully saturated (0.14 S/m) beach sand. Because the instrument's cell constant is calibrated for free solution, readings taken in granular samples indicate the conductivity of the water within the sample rather than a calibrated bulk conductivity; the bulk conductivity of the saturated sand is lower by approximately the formation factor, of order 0.03–0.06 S/m for a porosity of 0.4. These measurements provide context for interpreting the depth limitations of the GPR data at this site, discussed further in Section 3.

A dense three-dimensional GPR survey was the primary geophysical method employed. A Sensors and Software pulseEKKO system with SmartCart and 250 MHz antennas was used to collect common-offset data. The 2018 campaign comprised an initial set of sparse profiles, providing an early characterisation of the ground ice geometry along selected lines parallel to the cliff face. The 2023 and 2024 campaigns extended this to a dense three-dimensional survey — an approach that, to our knowledge, has not previously been applied to characterise ground ice distribution in an active coastal permafrost setting. Approximately 200 profiles were collected across both years, oriented perpendicular to the cliff face with a cross-line spacing of 0.5 m and an inline trace spacing of 0.05 m, producing a sub-metre spatial resolution sufficient to capture metre-scale variability in the ground ice surface. Several additional profiles were collected parallel to the cliff face between the cliff base and the sea, providing along-shore context. Positional and elevation information for the 2023 and 2024 GPR profiles was obtained using a real-time kinematic (RTK) GPS system (Emlid Reach RS2+), enabling the data to be positioned and gridded in three dimensions rather than interpreted as isolated two-dimensional sections. Positions for the 2018 profiles were recorded with a handheld GNSS receiver; elevations for these profiles were derived from a contemporaneous photogrammetric digital elevation model (DEM) rather than from the receiver, whose vertical accuracy was insufficient for this purpose. Common midpoint (CMP) gathers with a step size of 0.05 m were acquired at selected locations in 2023 and 2024 to derive electromagnetic velocity profiles of the subsurface, which were used to convert two-way travel times to depth. No CMP gathers were acquired in 2018. The velocity for that year was instead obtained from eight diffraction hyperbolae fitted along a 275 m transect, which returned values between 0.070 and 0.120 m/ns with a mean of 0.089 m/ns and a standard error of 0.007 m/ns; a value of 0.084 m/ns was adopted, within one standard error of that mean. The fitted velocities decrease with two-way travel time ($r = -0.74$, p=0.04), as would be expected if saturation increases with depth and towards the sea, but the trend is not robust to removal of individual hyperbolae and a single velocity was therefore retained for 2018. The consequences of this choice are quantified in Section 3.

Passive seismic data were acquired alongside the GPR measurements in both the 2023 and 2024 campaigns, using a custom-built low-cost acquisition system connected to three-component geophones, developed as an *in-situ* monitoring tool suitable for long-term community-based permafrost observation (Khan et al., 2024). The system has a Nyquist cut-off frequency of 400 Hz,

https://doi.org/10.5194/egusphere-2026-5431
Preprint. Discussion started: 22 September 2026

(a) Pre-storm: 18 August 2024

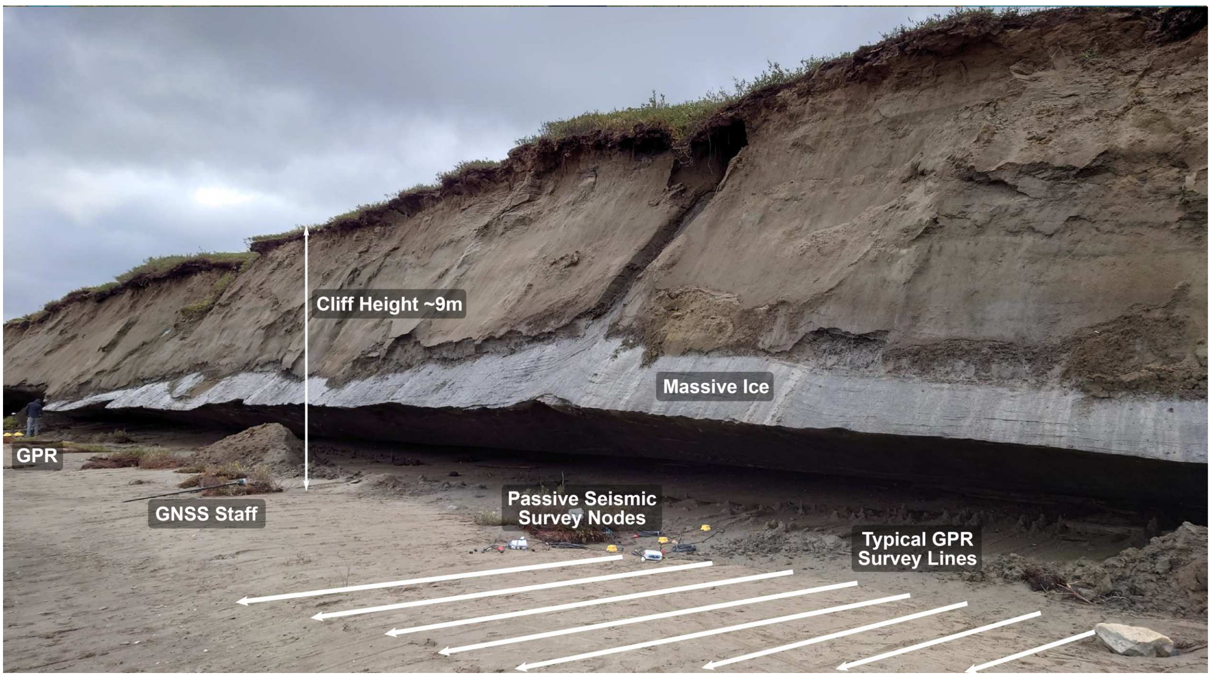

(b) Post-storm, with survey deployment: 21 August 2024

Figure 2. The north-west cliff face of Qikiqtarjuak (Tuktoyaktuk Island) before (a) and after (b) a storm between 18 and 21 August 2024, showing thermomechanical undercutting and fresh exposure of massive ice over three days. The exposed ice displays clear internal layering. In (b), the GPR system, GNSS staff, passive seismic nodes and dense GPR grid tracklines are visible on the beach, illustrating the survey deployment geometry. Photographs by the authors.

https://doi.org/10.5194/egusphere-2026-5431
Preprint. Discussion started: 22 September 2026

giving it sensitivity to significantly higher frequencies than most commercial off-the-shelf instruments. Three geophone nodes were deployed at 1 m spacing along lines oriented perpendicular to the cliff face, matching the GPR profile direction, with a record length of 10 minutes per location; the nodes were then moved progressively along the line to build up profiles. The Horizontal-to-Vertical Spectral Ratio (HVSR) method (Nakamura, 1989) was applied to the recorded data to estimate the thickness of the active layer at each node location, the resonant frequency f_0 of the layer giving its thickness as $H = V_s/4f_0$ for shear wave velocity V_s. In 2024, nodes close to the cliff base also showed secondary spectral peaks consistent with deeper interfaces within the ice body.

Two trial pits were excavated near the cliff base in 2023, on 10 and 16 August and 4.2 m apart, reaching wet sand throughout to depths of 1.16 and 0.62 m respectively. In both, the material at the base of the pit was visually identified as massive ice rather than ice-bonded sediment. This provides direct confirmation, for the landward part of the beach where the ice is shallowest, that the upper surface of the massive ice lies at the base of the thawed sand; further seaward its identification rests on the geophysical data alone.

Active layer thickness (ALT) probing was carried out in 2024 at regular intervals across the survey area using a steel rod with a handle, allowing measurements to depths of up to 1.33 m. Probe refusal was interpreted as contact with the upper surface of the massive ice, consistent with the 2023 trial pit observations, so that the ALT measurements serve as direct ground truth for the GPR reflector. Their locations were recorded using the RTK GPS system, which was also used to register all passive seismic node positions, ensuring that GPR, passive seismic, and ALT data could be compared on a common spatial framework.

The Stefan equation (Stefan, 1891) was used to predict the expected seasonal thaw penetration depth at the time of each survey campaign, providing an independent estimate of active layer thickness against which the GPR, passive seismic, and ALT measurements could be validated. The equation is given by:

$$X = \sqrt{\frac{2kI_t}{L}} \tag{1}$$

In Eq. (1), X is the thaw depth (m), k is the thermal conductivity of the thawed soil (W m^{-1} °C^{-1}), I_t is the surface thawing index (degree-seconds), and L is the volumetric latent heat of fusion of the soil (J m^{-3}). In this form the equation assumes that all energy delivered at the surface goes into latent heat of melting, that conduction is the dominant heat transfer process, that the thaw front is a sharp boundary, that the density of the thawing layer is constant, and that heat flux from the underlying permafrost is negligible. An n-factor of 1.0 was applied, appropriate for a bare wet beach sand surface with no vegetation cover (Lunardini, 1978), a thermal conductivity of 1.2 W m^{-1} °C^{-1} for saturated sand (Williams and Smith, 1991), and a volumetric latent heat of 2.14×10^8 J m^{-3} (assuming a dry bulk density of 1600 kg m^{-3} and a volumetric water content of 0.40). A sensitivity analysis across plausible ranges of thermal conductivity (1.0–1.5 W m^{-1} °C^{-1}), volumetric water content (0.35–0.45) and thawing n-factor (1.0–1.3, spanning reported values for bare granular surfaces) was also performed; thaw depth scales as the square root of the n-factor, so the upper bound increases predicted depths by 14%.

Thawing indices were calculated by summing daily mean air temperatures above 0 °C from 1 January to the survey date in each year, using records from Environment and Climate Change Canada station 2203911 (Tuktoyaktuk A). For the 2023

https://doi.org/10.5194/egusphere-2026-5431
Preprint. Discussion started: 22 September 2026

campaign (survey date 20 August) and 2024 campaign (survey date 18 August), measured daily data were available, with two days missing in each of those years, yielding thawing indices of 1,103 °C days and 882 °C days respectively. For the 2018 campaign (survey date 18 August), daily data were unavailable from station 2203911 for the January–August period; the thawing index was therefore estimated by applying the mean historical seasonal fraction (0.76 ± 0.05, derived from 17 complete years of record at the adjacent long-term station 2203914 for the period 1996–2016) to the published annual thawing index of 752 °C days (Government of Canada, 2025), giving an estimated Jan–Aug thawing index of approximately 574 °C days. The Stefan equation predicts seasonal thaw penetration depths of approximately 0.75 m (sensitivity range 0.64–0.89 m) at the time of the 2018 survey, 1.03 m (sensitivity range 0.89–1.24 m) at the time of the 2023 survey, and 0.93 m (sensitivity range 0.80–1.11 m) at the time of the 2024 survey. Comparison of these predictions with the active layer thicknesses derived from the geophysical surveys is discussed in Section 3.

To assess whether a multi-year trend in seasonal thaw penetration could itself account for part of the observed ground ice degradation, thawing indices were additionally calculated for each intervening year (2019–2022) from daily records at station 2203911. For this purpose a fixed 1 January–20 August window was used for every year, so that years are directly comparable; this differs by up to two days from the survey-date windows used for the Stefan predictions above. Data gaps were short — at most 12 missing days in any year (2020) and never more than five consecutive days — and were filled by linear interpolation. The resulting indices are 571.5 °C days for 2018 (estimated as above), 712.7, 693.0, 837.6 and 814.6 °C days for 2019–2022 respectively, 1,102.5 °C days for 2023, and 906.6 °C days for 2024. These were used to test for a trend in Stefan-predicted thaw depth over the study period, discussed alongside the degradation rate results in Section 3.

3 Results and Discussion

Processing and visualisation of the GPR data was carried out using Geolitix (https://www.geolitix.com/) software. A processing workflow consisting of time zero correction, dewow, manual gain, background removal, band-pass filtering, and migration was applied to all profiles. A static topographic correction was applied to all profiles using RTK GPS elevation data to account for beach surface relief. Electromagnetic velocities in the overlying wet sand between the beach surface and the top of the ground ice were derived from the CMP gathers and validated against the ALT probing measurements for 2023 (0.073 m/ns, $\epsilon_r = 17$) and 2024 (0.075 m/ns, $\epsilon_r = 16$). For 2018, where neither CMP gathers nor ALT probing are available, the velocity of 0.084 m/ns ($\epsilon_r = 12.7$) was determined from diffraction hyperbolae as described in Section 2.

Fig. 3 shows representative GPR B-scans from the 2023 and 2024 campaigns, both recorded perpendicular to the cliff face on the north-west coast. In both panels a clear reflector representing the top surface of the buried massive ice (amber line) is visible, dipping away from the cliff base towards the sea. In the 2023 profile (Fig. 3a), the ice surface dips from approximately 0.9 m depth at the cliff base to greater than 1.9 m depth at 7 m along the profile, indicating a slope of approximately 1:7 away from the cliff. In the 2024 profile (Fig. 3b), the ice surface dips from approximately 0.38 m depth at the cliff base to 1.37 m depth at 4 m along the profile, indicating a slope of approximately 1:4 away from the cliff. The notably shallower ice surface in 2024 relative to 2023 is consistent with the lower thawing index in 2024 (882 vs. 1,103 °C days), which produced a

https://doi.org/10.5194/egusphere-2026-5431
Preprint. Discussion started: 22 September 2026

shallower active layer and consequently a shallower apparent depth to the ice surface. The GPR signal becomes undetectable at depths of approximately 1.9 m in 2023 and 1.2 m in 2024, consistent with high attenuation in the increasingly saturated sand at greater distances from the cliff. The shallower penetration in 2024 despite a marginally lower relative permittivity ($\epsilon_r = 16$) than in 2023 ($\epsilon_r = 17$) most likely reflects a more electrically conductive overburden in 2024, since GPR attenuation is governed primarily by bulk conductivity rather than permittivity; the measured conductivities at this site (Section 2), which rise by a factor of thirty between partially and fully saturated sand, indicate that saturation state is a dominant control on signal attenuation. A second, deeper reflector is visible near the cliff base in the 2024 profile (deep orange line). Using velocities of 0.075 m/ns for the overlying wet sand and 0.168 m/ns for pure ice ($\epsilon_r = 3.2$), it lies approximately 4.8 m below the top of the ice. Whether this represents the base of the ice body or an impedance contrast within it cannot be established from the radar alone: massive ice exposed in the cliff face at this site displays clear internal layering (Fig. 2b), and such layering is capable of generating reflections at depths shallower than the true base. The same ambiguity applies to the secondary spectral peaks in the passive seismic data discussed below, and we treat 4.8 m as a minimum estimate of ice thickness rather than a measurement of it. Passive seismic HVSR top-of-ice depths (red circles) are overlaid in both panels, and active layer probe measurements (cyan circles) are shown in the 2024 panel only, all with individual error bars. Their consistency with the GPR reflector supports its interpretation as the top of the ice body in both years, and trial pits near the cliff base confirm directly that the probe meets massive ice rather than ice-bonded sediment at refusal (Section 2).

Passive seismic HVSR measurements were made concurrently along the same profiles in both 2023 and 2024, providing independent constraints on the active layer thickness along lines approximately collocated with the GPR surveys. Along both profiles, all nodes show a single spectral peak in the range 10–70 Hz corresponding to the base of the active layer in the sand. In 2024, secondary peaks at approximately 135–151 Hz are observed in the nodes closest to the cliff base (Fig. 4); these most likely correspond to a deeper interface within or at the base of the massive ice body, though comparison with the GPR data suggests these may be detecting an intermediate impedance contrast within the ice rather than the true base. Shear wave velocities for the sand were not measured directly but were calibrated against the 2024 ALT probing depths at co-located nodes, giving values from 84.2 m/s near the sea to 98.1 m/s near the cliff — low values, consistent with loose, saturated, unconsolidated sand — and the same velocity–position relationship was applied to the 2023 profile. Depths to the secondary peaks were derived using a shear wave velocity of 1,800 m/s, appropriate for massive ice; the resulting contrast of more than an order of magnitude between sand and ice is what makes the top of the ice a strong HVSR reflector. Because the velocities are calibrated in this way, the HVSR depths are not independent of the ALT measurements, and the agreement between them is a closure check on the calibration rather than corroboration. The HVSR depths are nonetheless independent of the GPR, sharing neither an instrument nor a velocity model with it, and their agreement with the GPR reflector in both survey years (Fig. 3) supports the interpretation of that reflector as the top of the massive ice.

The combination of dense GPR data, passive seismic measurements, and ALT probing enabled construction of a three-dimensional surface model of the top of the massive ice body across the surveyed area (Figs. 5 and 7). The model reveals a consistently dipping ice surface from approximately 0.4 m at the cliff base to approximately 2 m at the seaward extent, with considerable along-shore variability in both depth and surface geometry that is only resolvable through the dense three-

https://doi.org/10.5194/egusphere-2026-5431
Preprint. Discussion started: 22 September 2026

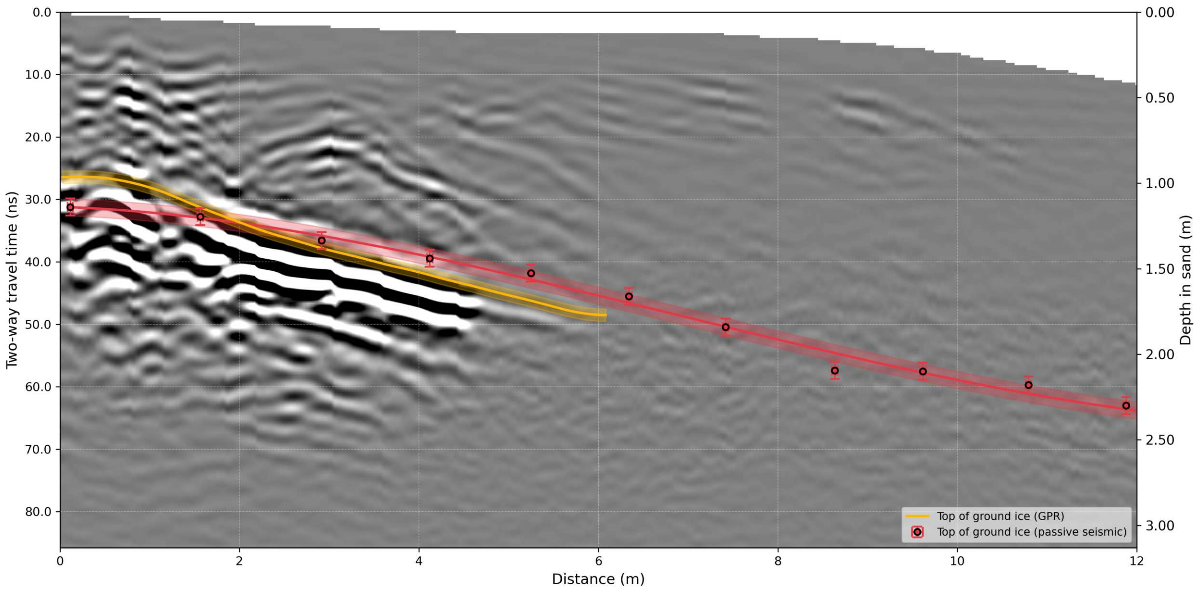

(a) August 2023

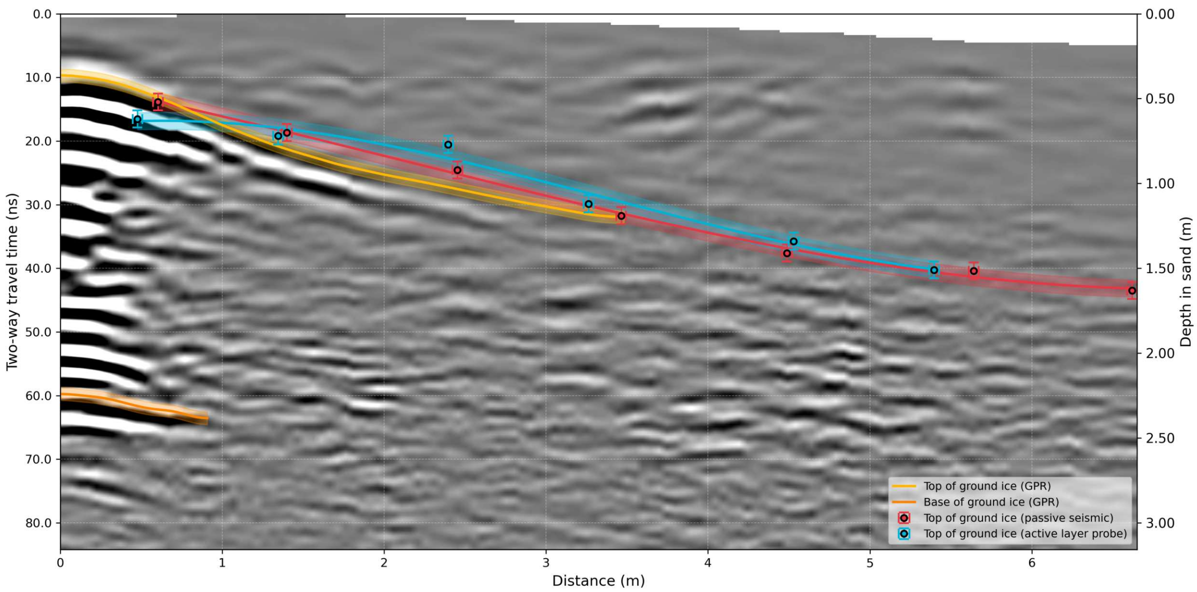

(b) August 2024

Figure 3. GPR B-scans recorded perpendicular to the cliff face on the north-west coast of Qikiqtarjuak (Tuktoyaktuk Island), with static topographic corrections applied using RTK GPS elevation data. The top of the ground ice is picked in amber and, in (b), a deeper reflector in deep orange, which may be the base of the ice body or an internal impedance contrast. Passive seismic HVSR top-of-ice depths (red circles) are overlaid in both panels; active layer probe measurements (cyan circles) appear in (b) only. Error bars are ± 0.05 m vertical and ± 0.03 m horizontal. The right-hand depth axis assumes the wet-sand velocity and is therefore valid only for reflectors within the active layer, not within or below the massive ice.

https://doi.org/10.5194/egusphere-2026-5431
Preprint. Discussion started: 22 September 2026

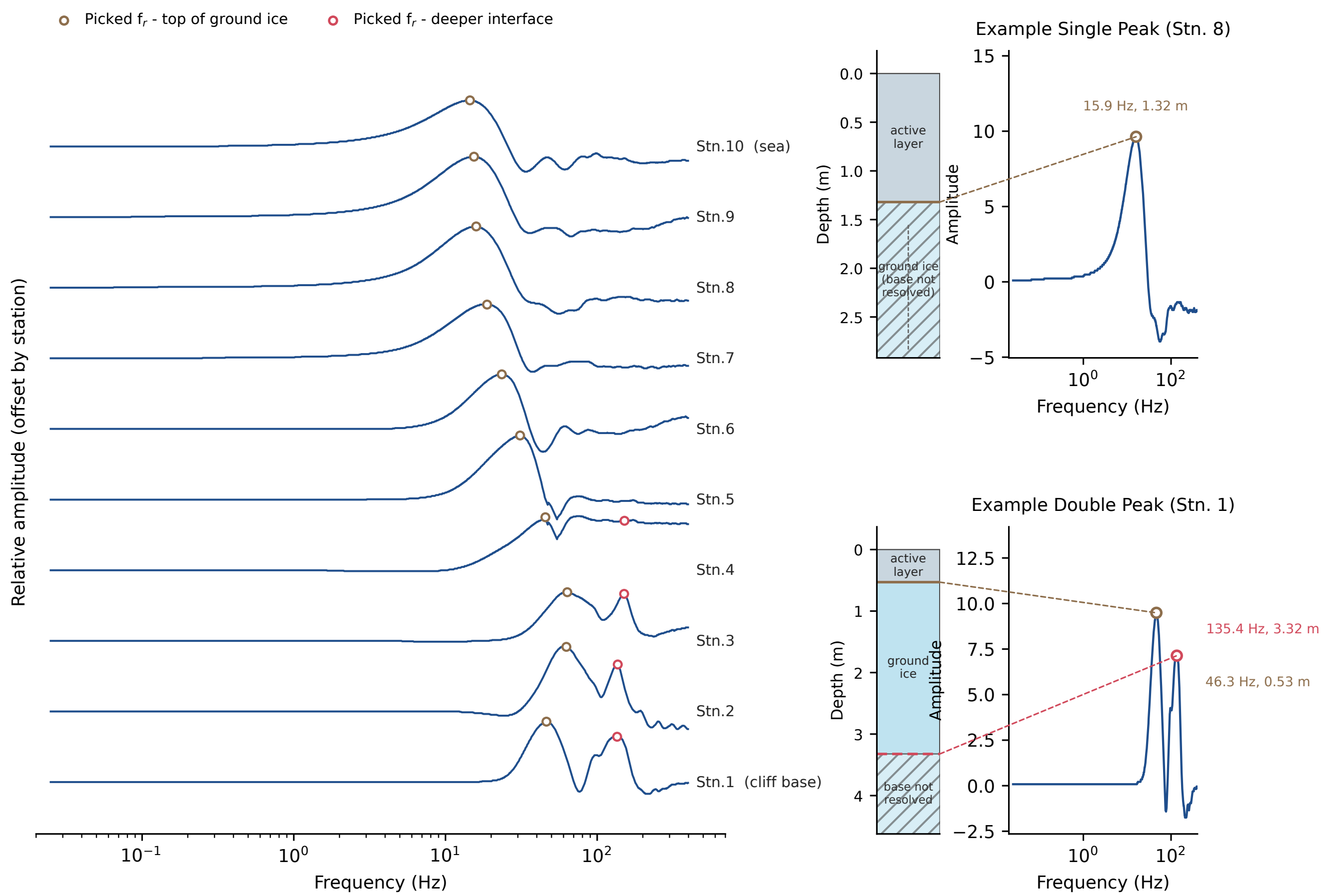

Figure 4. Passive seismic HVSR spectral curves recorded perpendicular to the cliff face, from the sea (top trace) to the cliff base (bottom trace) at 1 m spacing, August 2024; equivalent 2023 curves are not shown. The single peak at 10–70 Hz corresponds to the base of the active layer in the sand. Secondary peaks near 150 Hz in the traces closest to the cliff correspond to a deeper interface within, or at the base of, the massive ice. Depths to the active layer base were estimated using shear wave velocities calibrated against co-located active layer probe measurements; those to the secondary peaks assume 1,800 m/s for massive ice.

https://doi.org/10.5194/egusphere-2026-5431
Preprint. Discussion started: 22 September 2026

dimensional survey approach. The landward displacement of the 2024 survey footprint relative to 2023, visible in Fig. 5, is itself a qualitative indicator of the scale of cliff retreat between the two seasons; the beach had narrowed sufficiently that the 2023 and 2024 grids share minimal overlap, precluding a direct year-on-year degradation rate comparison between those campaigns.

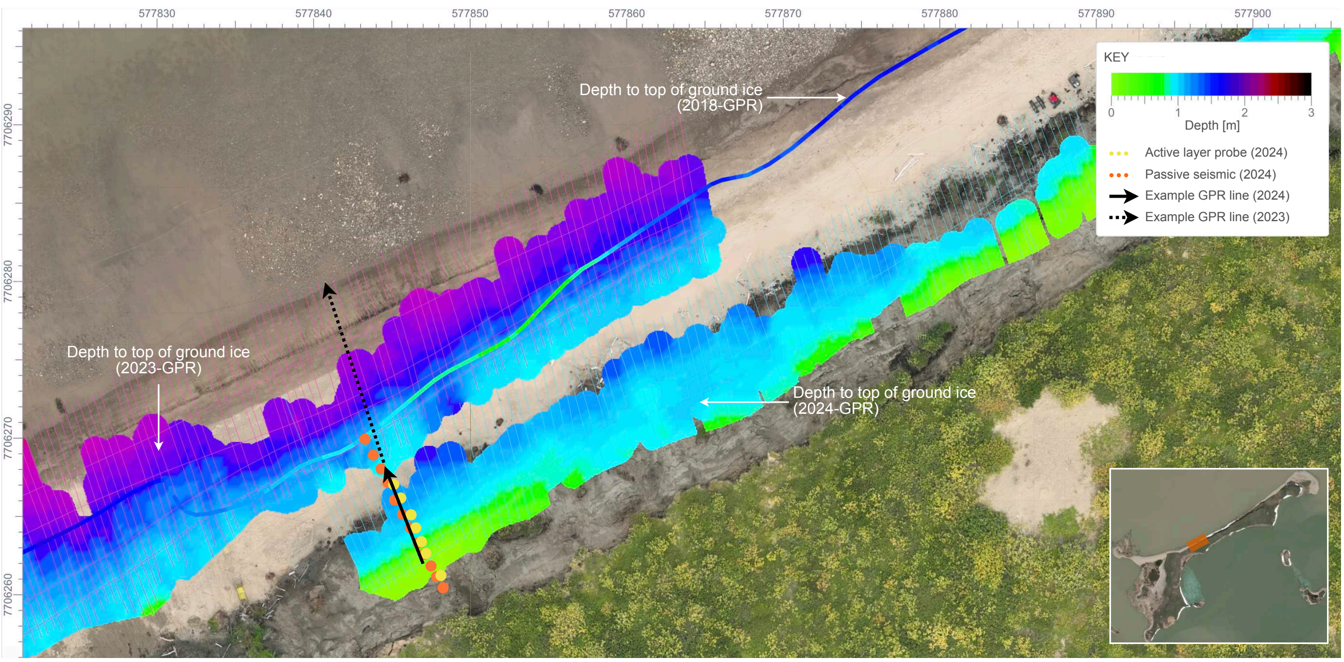

Figure 5. Depth to the top of the ground ice across the north-west coast of Qikiqtarjuak (Tuktoyaktuk Island) from the 2018, 2023 and 2024 GPR surveys, on drone imagery acquired in August 2024. Colour indicates depth below the beach surface (green = shallow, purple = deep). Active layer probe (yellow) and passive seismic (orange) measurements from 2024 are overlaid. Inset locates the survey area on the island; inset basemap imagery: Esri, Maxar, Earthstar Geographics.

Ground ice degradation rates were calculated by comparing the depth to the top of the ground ice surface between the 2018 and 2023 GPR datasets. The 2018 dataset comprised a single profile oriented approximately parallel to the cliff face at approximately mid-beach, which intersects the 2023 dense survey grid. A 44.6 m section of that profile was used. The remainder of the overlapping profile, closest to the cliff, was excluded on positional grounds: handheld GNSS elevations there departed from the contemporaneous photogrammetric DEM with a scatter of 3.2 m, against 0.6 m over the retained section, consistent with multipath from the adjacent ice cliff face. The extent of the comparison was therefore set by positional accuracy rather than by any property of the GPR data. For each point along the 2018 profile, the nearest corresponding point in the 2023 dataset was identified using a Euclidean distance threshold of 0.5 m in the horizontal plane. Where a match was found within this threshold, the depth difference between the two measurements was divided by the five-year interval between surveys to give a degradation rate in cm yr^{-1}; this yielded 933 matched point pairs across the transect. To examine the relationship between degradation rate and initial ice depth, the 2018 depth values were grouped into bins of 3 cm — a width chosen to balance

https://doi.org/10.5194/egusphere-2026-5431
Preprint. Discussion started: 22 September 2026

resolution of the depth-dependence against averaging of pick-to-pick scatter — and the mean degradation rate calculated for each bin. Of the 28 bins so formed, one, at the greatest overburden thickness sampled, returned a mean rate that was negative and indistinguishable from zero; it is excluded from the exponential fit below, which is defined only for positive rates, and its exclusion changes the mean rate across the remaining bins by 0.2 cm yr^{-1}.

The total uncertainty in the degradation rate calculation reflects contributions from two principal sources. First, GPR reflector picking uncertainty of $\pm 5\%$ in depth — appropriate for the strong, high-amplitude reflector produced by the massive ice surface — combines in quadrature between the two independent surveys, giving $\pm\sqrt{2} \times 0.05 \times d$ at depth d, or ± 71 mm at a typical ice depth of 1 m. Because reflector depths were picked in two-way travel time and converted to depth below the local beach surface, GPS vertical accuracy does not propagate into the depth difference between surveys. Second, changes in beach surface elevation between the two campaigns were assessed directly by differencing contemporaneous photogrammetric DEMs at each GPR trace position along the transect; the mean surface change was -0.7 ± 8.0 cm, indistinguishable from zero at DEM accuracy, confirming that the measured depth differences reflect genuine lowering of the ice surface rather than redistribution of beach sediment. Propagating these two sources in quadrature gives a combined depth uncertainty of approximately ± 107 mm over the five-year comparison period, equivalent to ± 2 cm yr^{-1}. The 2018 electromagnetic velocity contributes a third, systematic uncertainty which is reported separately because a single value scales all 2018 depths together and therefore displaces the whole relationship rather than adding scatter to it: the standard error of 0.007 m/ns on the mean of the eight hyperbola fits propagates to ± 0.6 cm yr^{-1} on the mean degradation rate and ± 9 cm on the fitted decay length reported below. Velocities for 2023 and 2024, derived from CMP gathers, are considered robust by comparison. This confirms that the mean degradation rate and the high rates observed for shallow ice are robust and well above the measurement noise floor. The combined uncertainty grows with depth, reaching ± 2.8 cm yr^{-1} at an overburden thickness of 1.65 m; degradation rates at the deeper end of the transect, where rates fall below ~ 2 cm yr^{-1}, therefore approach the uncertainty threshold and should be interpreted with caution. Horizontal error bars on Fig. 6 reflect the combined GPR picking uncertainty of $\pm\sqrt{2} \times 0.05 \times d$ at each point's initial (2018) overburden depth d; vertical error bars reflect the full combined depth uncertainty (picking and beach-change terms in quadrature, as derived above) propagated to a rate over the five-year interval.

The stability of the beach surface is itself informative. Melting 30 cm of nearly pure ice should leave a void of comparable volume, and without resupply the overburden would settle into it, lowering the beach by a similar amount. No such lowering is observed: the DEM difference excludes 30 cm of subsidence at more than three standard deviations. The beach is therefore replenished at close to the rate at which ice is lost beneath it. Collapse of the cliff face is the obvious source — Fig. 2 shows several metres of material delivered to the beach in three days — implying that beach thickness is maintained in approximate equilibrium between supply from the retreating cliff and accommodation of the space vacated by melting ice. This assumes an excess ice fraction near unity; were the ice to contain appreciable sediment, the expected subsidence would fall proportionately.

Comparison of the 2018 profile with the 2023 dense survey data provides the first direct estimate of ground ice degradation rates in the near-shore coastal zone of Qikiqtarjuak (Fig. 6). Degradation rates vary with depth, ranging from values approaching the measurement uncertainty threshold for ice at depths greater than 1.6 m to 14 ± 2 cm yr^{-1} in the shallowest bin sampled, at 0.83 m, with a mean of 6 ± 2 cm yr^{-1} over the 3 cm bins spanning the transect. The depth-dependence follows an exponential

https://doi.org/10.5194/egusphere-2026-5431
Preprint. Discussion started: 22 September 2026

decay, $\dot{S}(h) = A\exp(-h/\delta)$, rather than a simple linear relationship: a fit with both A and the decay length δ parameters free explains 89% of the variance in the binned data, comparable to a four-parameter piecewise-linear fit (91%) but with half the free parameters. The fitted decay length constrains the periodicity of the surface forcing. For a periodic surface temperature oscillation of period T diffusing into a semi-infinite medium, the classical damping-depth solution to the heat conduction equation (Carslaw and Jaeger, 1959) gives a temperature amplitude decaying as $\exp(-h/\delta)$ with depth h, where $\delta = \sqrt{\kappa T/\pi}$ is the damping depth and κ the thermal diffusivity of the sand. Short-period signals are damped within a shorter depth than long-period ones. The observed quantity here is a degradation rate rather than a temperature, but the two share this decay length: by the Stefan condition at the ice surface, the rate of melting is proportional to the conductive heat flux arriving there, and the flux amplitude is proportional to the temperature gradient, which decays as $\exp(-h/\delta)$ with the same δ. A degradation rate declining exponentially with overburden thickness is therefore the expected signature of a periodic surface thermal signal, and its decay length carries the periodicity of that signal. Inverting for T using the thermal properties adopted for the Stefan calculation ($k_s = 1.2$ W m^{-1} °C^{-1}; an assumed volumetric heat capacity of 2.95 MJ m^{-3} °C^{-1}, giving $\kappa \approx 4.1 \times 10^{-7}$ m^2 s^{-1}) gives a forcing period of approximately 14 days. Propagating both the ranges of thermal conductivity and volumetric water content used in the Stefan sensitivity analysis (Section 2) and the systematic uncertainty in the 2018 velocity widens this to 7–27 days.

This band is diagnostic even though δ itself is not tightly constrained by the available thermal properties. It excludes the semi-diurnal and diurnal tidal constituents by factors of thirteen and seven respectively, and the annual cycle by a factor of thirteen in the opposite sense. It contains the 14.56-day spring–neap period at Tuktoyaktuk, derived by spectral analysis of Canadian Hydrographic Service water level predictions at station 06485, and the synoptic recurrence interval of the storms that inundate this beach; these two are not separable at the resolution of the present data. A semi-diurnal contribution to surface wetting is likely at this site, but cannot influence the observations reported here: with a damping depth of 7.6 cm, a semi-diurnal signal is attenuated by more than four orders of magnitude before reaching the shallowest measured overburden thickness of 0.79 m. The depth-dependence of degradation is therefore controlled by fortnightly-scale modulation of the surface thermal boundary condition, as the beach alternates between inundated and exposed states, rather than by a depth-invariant insulation effect. Meltwater released at the ice surface is too small a volume to saturate the overburden from below — at the highest observed rate it amounts to under 40% of the available pore volume per year, and under 5% at the deepest — so the saturation state governing the thermal properties of the sand is set from the surface rather than from beneath. Some scatter at intermediate depths may additionally reflect localised geological variability, or locally enhanced melting where meltwater from massive ice exposed in the cliff face drains across the beach surface.

The measured active layer thicknesses are broadly consistent with the Stefan equation predictions derived in Section 2. For 2023, the two trial pits excavated near the cliff base reached the ice surface at 1.16 and 0.62 m, bracketing the 2023 Stefan prediction of 1.03 m and its sensitivity range of 0.89–1.24 m. The 2023 passive seismic top-of-ice depths (Fig. 3a) are systematically deeper, ranging from 1.14 to 2.41 m across the beach profile, with the deepest exceeding the upper bound of the Stefan range by a factor of almost two. The Stefan equation therefore reproduces the thaw depth where direct excavation constrains it, near the cliff, but not the seaward end of the seismic profile. Whether that reflects a genuinely thicker active layer

https://doi.org/10.5194/egusphere-2026-5431
Preprint. Discussion started: 22 September 2026

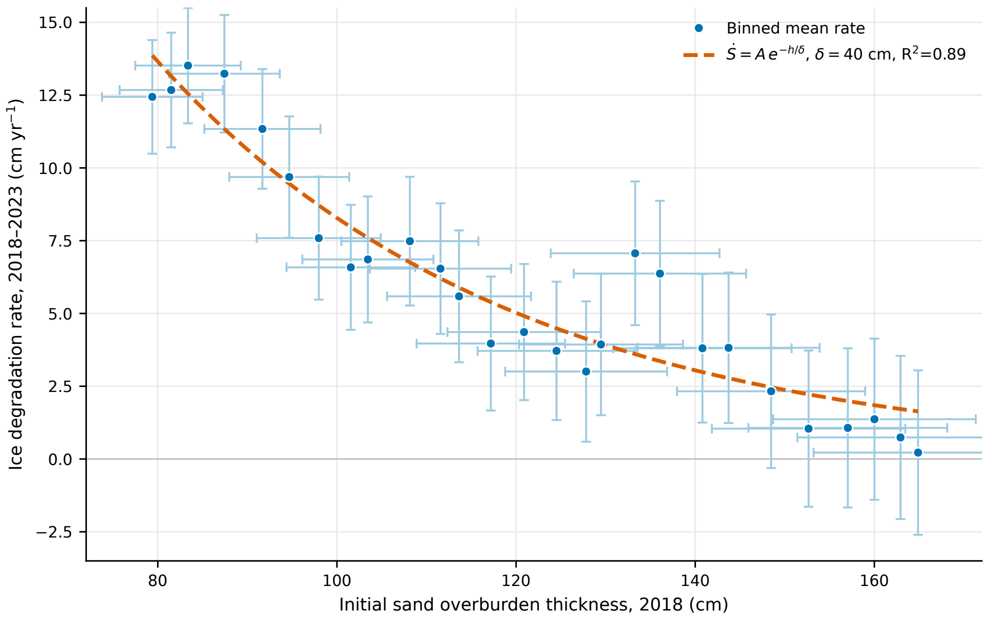

Figure 6. Ice degradation rate (2018–2023) against initial sand overburden thickness in 2018, along a single transect at mid-beach on the north-west coast of Qikiqtarjuak (Tuktoyaktuk Island). Points are mean rates within 3 cm overburden bins. Horizontal bars show the combined GPR picking uncertainty; vertical bars the full combined uncertainty, picking and beach-change terms in quadrature, propagated to a rate. The dashed line is a fitted exponential decay, $\dot{S} = A\exp(-h/\delta)$, with both the amplitude A and the decay length δ free.

seaward, where the beach surface falls and saturation increases, or an overestimate in the HVSR depths, cannot be resolved without direct measurements further from the cliff. The 2024 ALT probe measurements (Fig. 3b) ranged from 0.62 to 1.51 m with a mean of 1.01 m, in excellent agreement with the 2024 Stefan prediction of 0.93 m (sensitivity range 0.80–1.11 m), and the 2024 passive seismic top-of-ice depths ranged from 0.52 to 1.63 m across the profile, also broadly consistent. In 2018, no independent ALT or passive seismic measurements were made, but the GPR-derived active layer depths are consistent with the 2018 Stefan prediction of 0.75 m (sensitivity range 0.64–0.89 m). The notably deeper active layer in 2023 relative to 2024 is directly visible in Fig. 3, and is consistent with the higher thawing index in 2023 (1,103 vs. 882 °C days), confirming that seasonal thaw penetration at the time of the surveys was driven primarily by conductive heating.

The relationship between seasonal thaw and permanent ice loss requires care. The Stefan equation predicts the depth of conductive seasonal thaw, a quantity validated here by the GPR, ALT and passive seismic measurements. Thawed sediment then refreezes each winter, and the freezing index at this site (3,900–4,400 °C days, against a thawing index of 1,100–1,400) is more than sufficient to refreeze the full active layer. What refreezes, however, is pore water within the sand; the massive ice that melted is not restored, since the meltwater drains or refreezes as pore ice. The upper surface of the ice body therefore descends monotonically to the greatest depth the thaw front has reached, and the rate measured here is the rate at which that maximum thaw depth increases rather than a difference between thaw and refreeze. Snow cover modulates the winter regime but does

https://doi.org/10.5194/egusphere-2026-5431
Preprint. Discussion started: 22 September 2026

not alter this conclusion: mean depths of 10.2–17.1 cm over the three winters for which records exist at station 2203914 give a thermal resistance comparable to 0.2–0.3 m of beach sand, small against the 0.8–1.7 m of overburden, and leave refreezing complete. Snow on this narrow, exposed and periodically inundated surface is likely thinner again.

Extending the thawing index record across the intervening years reveals a significant increasing trend in Stefan-predicted thaw depth over the interval spanned by the degradation measurement (2018–2023: 4.9 ± 0.4 cm yr^{-1}, R^2=0.86, p=0.008, the uncertainty propagating the seasonal fraction used to estimate the 2018 index), equivalent to 5.8 ± 0.5 cm yr^{-1} between the two survey years and closely comparable to the observed mean rate. The interval was chosen to match the degradation measurement itself. Excluding the estimated 2018 index leaves the slope almost unchanged (4.7 cm yr^{-1}) but reduces the significance to p=0.05, and extending the regression to include the cooler 2024 season lowers it to 3.8 cm yr^{-1} (p=0.010); the trend is therefore robust in sign and order of magnitude but sensitive in value to the years included, and the correspondence with the measured rate should be read as order-of-magnitude rather than quantitative. Active layer thickening under rising thawing indices — a conductive response to warming requiring no additional heat source — is thus a plausible primary driver of the permanent ice loss measured here.

The two mechanisms account for different aspects of the observation and are complementary rather than competing. The trend in thawing indices accounts for the magnitude of the mean rate, whereas the persistence of measurable degradation at overburden thicknesses of 1.4–1.65 m, below the maximum conductive thaw depth predicted in any survey year, requires a process capable of transmitting a thermal signal beneath the seasonal thaw front; the exponential depth-dependence and its implied fortnightly forcing period provide one. Advective heat transfer from periodic seawater inundation is therefore best understood as shaping the depth-distribution of ice loss rather than driving its magnitude. Its thermal effect is in any case moderated by the proximity of the Mackenzie Delta, which suppresses nearshore salinities to 10–30 ppt in summer (Hopky et al., 1990). Our own measurements sit at the lower end of that range and indicate fresher conditions again within the beach: a seawater conductivity of 1 S/m corresponds to roughly 10–14 ppt at summer temperatures, while water in the saturated sand is some seven times less conductive again — consistent with dilution by meltwater from the exposed cliff ice and by terrestrial groundwater drainage. The resulting freezing point depression is approximately 0.5–0.8 °C nearshore and less within the beach, against 1.9 °C at open-ocean salinity, so salt-driven acceleration of thaw is correspondingly reduced.

The cross-sectional profile and three-dimensional perspective view in Fig. 7 place the GPR ice surface measurements in their full geomorphological context by combining them with the cliff face geometry derived from photogrammetric surveys acquired in August 2024. The profile (upper panel) reveals the geometric relationship between the cliff top at approximately 9.4 m elevation, the beach surface, and the GPR-derived ice surface beneath. Along this section the ice lies approximately 0.8 m below the beach at the cliff base, deepening to approximately 1.7 m at the seaward limit of GPR coverage — a gradient of approximately 1:5, within the 0.4–2 m range spanned by the wider survey — and passes below mean sea level approximately 2.4 m seaward of the cliff base. This cross-sectional geometry can be placed alongside the subsea IBPT documented at 5 m below sea level just 120 m offshore (Erkens et al., 2025), which deepens to around 20 m below sea level at 250–800 m offshore, a mean IBPT gradient of approximately 1:32. The two datasets do not, however, map the same horizon. The GPR resolves the upper surface of the massive ice body, whereas the marine ERT resolves the IBPT, the depth at which pore ice first occurs.

https://doi.org/10.5194/egusphere-2026-5431
Preprint. Discussion started: 22 September 2026

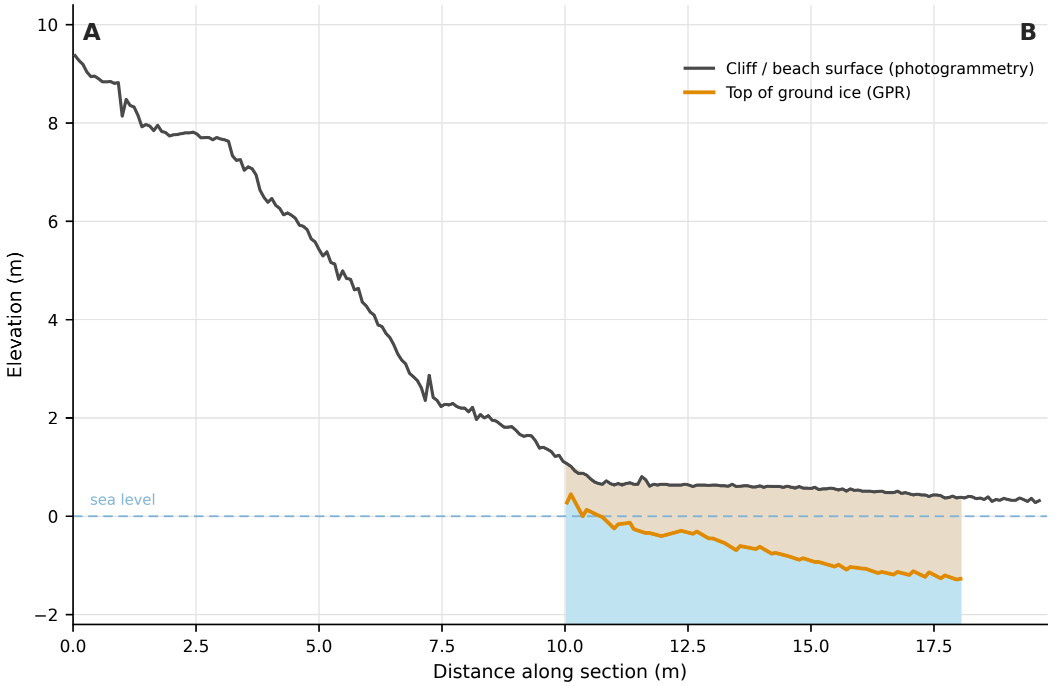

(a) Cross-section along A–B

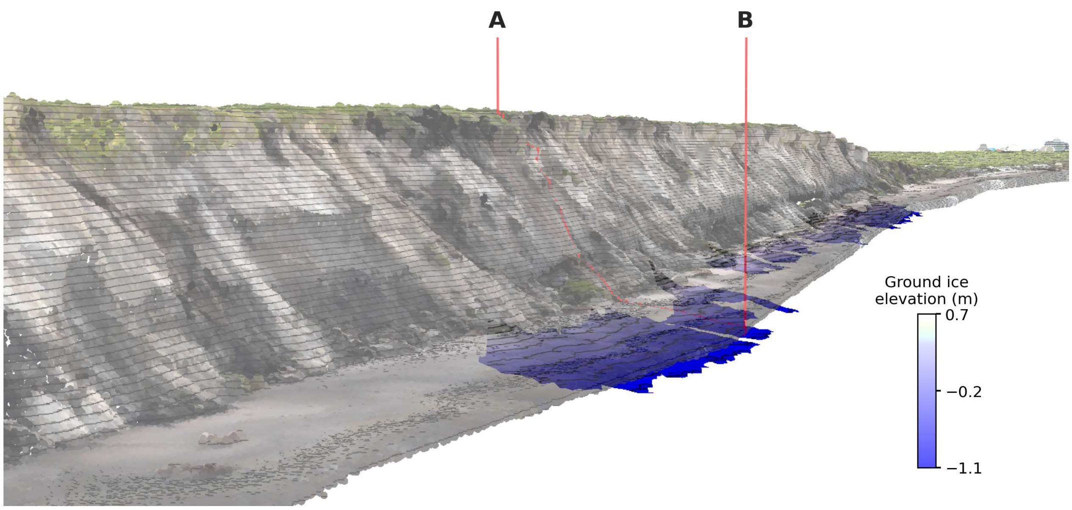

(b) Three-dimensional perspective view

Figure 7. Cross-section and three-dimensional perspective view of the north-west cliff face and beach of Qikiqtarjuak (Tuktoyaktuk Island), August 2024. (a) Section A–B at true scale, with no vertical exaggeration: the photogrammetric cliff and beach surface (dark line) and the GPR-derived top of the massive ice (amber). Sand shading marks the overburden between them; pale blue the ice body, whose base is not resolved here. (b) The same ice surface in spatial context, coloured by elevation, beneath the photogrammetric cliff model rendered semi-transparent so the ice is visible through the beach. Red leaders and the dashed trace mark section A–B.

https://doi.org/10.5194/egusphere-2026-5431
Preprint. Discussion started: 22 September 2026

Where massive ice forms the top of the frozen column beneath a seasonally thawed active layer, the two surfaces effectively coincide; trial pits near the cliff base establish that this is the case there, the probe meeting massive ice directly beneath the thawed sand. Where frozen sediment overlies the massive ice, the IBPT lies above it, and neither dataset constrains how large that separation becomes offshore. The comparison therefore relates two surfaces bounding the same degrading permafrost body rather than a single mapped horizon.

With that caveat, the terrestrial ice surface gradients of approximately 1:4 (2024) and 1:7 (2023) are considerably steeper than the subsea value, but not inconsistent with it: the GPR B-scans sample the ice geometry close to the actively eroding cliff where the surface is steep and recently exposed, whereas the IBPT gradient integrates the longer-term inundation and degradation history over much greater offshore distances. Together the two describe a surface that is steep near the shoreline and flattens progressively offshore, indicating continuity of the permafrost body across the coastline even though the surfaces mapped on either side of it are not identical.

The mean terrestrial ground ice degradation rate of 6 ± 2 cm yr^{-1} falls within the range of subsea IBPT degradation rates from marine ERT surveys on the northern side of the island (Erkens et al., 2025), where the mean is 5.3 ± 4.0 cm yr^{-1} with borehole-constrained values of 6.6 ± 3.0 and 10.2 cm yr^{-1} nearer the shore, the latter quoted without an uncertainty. Those rates are inferred by combining a single season of ERT data with historical shoreline positions rather than from repeat geophysical survey, and the quoted uncertainty is wide enough to encompass most plausible rates, so the agreement is weak evidence taken alone; it is the coincidence of comparable rates with a depth-dependence of the same sense — faster degradation at shallower depths in both datasets — that is suggestive of shared control. Cliff retreat rates of approximately 5 m yr^{-1} on the north-west shore, far exceeding the vertical ice degradation rate, are the dominant mechanism of volumetric ice loss at the site and confirm that the beach on which the geophysical surveys were conducted is a rapidly narrowing, transient feature. Together, the comparable degradation rates across the shoreline and the geometric continuity of the ice surface from beach to seafloor are consistent with the same processes — conductive warming under rising air temperatures, with periodic seawater inundation modulating the depth-distribution of ice loss — operating continuously across the terrestrial-to-marine transition zone.

Several limitations bear on the interpretation of these results. The degradation rates derive from a single 44.6 m transect at mid-beach rather than from a spatially distributed comparison, and the mean quoted is taken over 3 cm bins of overburden thickness, each weighted equally irrespective of how many observations it contains; it is therefore a mean over the observed depth range at mid-beach rather than a spatial mean across the survey area. The 2018 electromagnetic velocity, obtained from diffraction hyperbolae rather than CMP gathers, remains the largest single systematic control on those rates. Neither snow depth nor sea ice extent was recorded at the site. Snow on a surface this exposed is expected to be thin and of secondary thermal importance, but interannual variation in either would modulate the thermal regime, and the length of the open water season in particular sets the period over which the beach can be inundated at all — the process on which the depth-dependence reported here depends. Finally, the depth to which the massive ice extends is not resolved, so the ice volumes implied by the mapped upper surface remain unconstrained from below.

https://doi.org/10.5194/egusphere-2026-5431
Preprint. Discussion started: 22 September 2026

4 Conclusions

Coastal permafrost degradation at Qikiqtarjuak (Tuktoyaktuk Island) is driven by a combination of processes operating across the terrestrial-to-marine transition zone, yet the distribution and geometry of the ground ice that underpins this system has, until now, remained uncharacterised in three dimensions. We have presented a combined geophysical and geomatic approach — dense three-dimensional GPR, passive seismic HVSR measurements, photogrammetric mapping, and active layer thickness probing with validation pits — to image the near-shore ground ice body on the north-west coast of the island across three field campaigns in 2018, 2023, and 2024.

The GPR data reveal a massive ice body whose upper surface dips from approximately 0.4 m depth at the cliff base to approximately 2 m at the seaward extent of the survey, with along-shore variability resolvable only through dense three-dimensional survey. The same geometry appears in both the 2023 and 2024 campaigns, and trial pits, probe depths and passive seismic depths agree with the GPR reflector where they overlap. Where the radar signal is lost in saturated sand, the passive seismic data extend the characterisation further seaward.

Repeat survey over the five-year interval yields the first direct measurements of coastal massive ice degradation at this site. Along a single mid-beach transect, rates range from values approaching the measurement uncertainty threshold for the deepest ice to 14 ± 2 cm yr^{-1} in the shallowest ice sampled, with a mean of 6 ± 2 cm yr^{-1} over the observed range of overburden thickness. The depth-dependence follows an exponential decay with a fitted decay length of 40 cm which, inverted through the thermal damping-depth relation, implies a surface forcing period of 7–27 days. That band excludes the diurnal tidal constituents and the annual cycle by roughly an order of magnitude in either direction, and contains both the spring–neap period and the synoptic storm recurrence interval.

Two mechanisms are at work, and they are complementary rather than competing. Refreezing each winter restores pore ice but not massive ice, so the ice surface descends monotonically to the greatest depth the thaw front reaches; the rising trend in Stefan-predicted thaw depth over the interval (4.9 ± 0.4 cm yr^{-1}) is comparable in magnitude to the measured rate, and accounts for it without invoking an additional heat source. Attenuation of the fortnightly wetting signal, by contrast, explains why measurable degradation persists below the maximum conductive thaw depth, and so governs how ice loss is distributed with depth rather than how much occurs. The mean terrestrial rate falls within the range of subsea ice-bearing permafrost table degradation rates reported offshore (Erkens et al., 2025), and the ice surface flattens progressively from 1:4–1:7 near the cliff to 1:32 offshore, indicating a permafrost body continuous across the coastline — though the terrestrial and subsea surveys resolve different surfaces within it, the top of the massive ice and the ice-bearing permafrost table respectively. Lateral removal by cliff retreat at approximately 5 m yr^{-1} nonetheless remains the dominant mechanism of volumetric ice loss, far exceeding the vertical rate.

Taken together, this study contributes a high-resolution, three-dimensional characterisation of ground ice in an active coastal permafrost setting — to our knowledge the first at this resolution in such a setting — and, from repeat survey of it, a measured control on how ground ice is lost with depth. Dense three-dimensional GPR combined with passive seismic methods and

https://doi.org/10.5194/egusphere-2026-5431
Preprint. Discussion started: 22 September 2026

ground truth is a practical tool for characterising ground ice in these settings, and could be applied at other vulnerable Arctic coastal sites.

These results also provide a baseline immediately prior to the installation of rock armour on the north-west beach in March 2025, and the expectation they set is specific: because armouring a beach alters the regime under which its surface is wetted, it should alter the depth-distribution of ice loss beneath it rather than simply arrest lateral retreat. More generally, where ground ice underlies a periodically wetted surface, the frequency of that wetting — not overburden thickness alone — governs how deeply ice is lost. That control is not static: lengthening open-water seasons and changing storm frequency will alter it, and the same reasoning is testable wherever repeat geophysical survey can resolve an ice surface beneath an ice-rich coast.

Data availability. The datasets reported here, comprising the processed GPR profiles, passive seismic HVSR spectra and picked resonance frequencies, active layer probe measurements and trial pit logs from the 2018, 2023 and 2024 field campaigns, together with the matched 2018/2023 point pairs and binned degradation rates underlying Fig. 6, and photogrammetric digital elevation models will be made available. Daily air temperature records used to compute the thawing indices are openly available from Environment and Climate Change Canada for stations 2203911 and 2203914 (https://api.weather.gc.ca). Water level predictions for Tuktoyaktuk are openly available from the Canadian Hydrographic Service for station 06485.

Author contributions. CW carried out the GPR fieldwork, processing and interpretation, and led the writing of the manuscript. JM carried out the passive seismic fieldwork and the HVSR processing and interpretation. GC contributed to the GPR fieldwork. MLim and RL carried out the active layer thickness probing, the photogrammetric surveys and the digital elevation model production. LM carried out the thermal analysis. DW led field logistics and community engagement and liaison. All co-authors contributed to the writing of the manuscript.

Competing interests. The authors declare that they have no competing interests.

Acknowledgements. The authors wish to acknowledge the Canada-Inuit Nunangat-United Kingdom (CINUK) Arctic Research Programme "Nuna – Changing ground conditions, Community resilience, technological solutions" (NE/X005658/1) project for enabling and supporting the field measurements used in this paper.

The authors wish to thank Craig Dixon and Patrick Baird on the Technical Support Team in the Faculty of Science and Environment at Northumbria University for their support with preparing the geophysical equipment for fieldwork.

Anthropic's Claude was used during preparation of this manuscript to assist with drafting and revision of the text, and to retrieve and process publicly available climate records. All data acquisition, interpretation, and scientific conclusions are the authors' own, and all outputs were checked and verified by the authors.

https://doi.org/10.5194/egusphere-2026-5431
Preprint. Discussion started: 22 September 2026

References

Angelopoulos, M., Westermann, S., Overduin, P., Faguet, A., Olenchenko, V., Grosse, G., and Grigoriev, M. N.: Heat and salt flow in subsea permafrost modeled with CryoGRID2, Journal of Geophysical Research: Earth Surface, 124, 920–937, https://doi.org/10.1029/2018JF004823, 2019.

Annan, A. P. and Davis, J. L.: Impulse radar sounding in permafrost, Radio Science, 11, 383–394, 1976.

Arcone, S. A., Lawson, D. E., Delaney, A. J., Strasser, J. C., and Strasser, J. D.: Ground-penetrating radar reflection profiling of groundwater and bedrock in an area of discontinuous permafrost, Geophysics, 63, 1573–1584, 1998.

Bradford, J. H., Siegfried, M., Follingstad, V., Hughson, K., Routt, A., Schmidt, B., Kubas, A., Quartini, E., Mullen, A., and Swidinsky, A.: Mapping the internal structure of Arctic pingos using ground-penetrating radar: results from the Pingo Canadian Landmark, in: Seventh International Conference on Engineering Geophysics, Al Ain, UAE, 16–19 October 2023, pp. 102–104, Society of Exploration Geophysicists, 2024.

Brosten, T. R., Bradford, J. H., McNamara, J. P., Zarnetske, J. P., Gooseff, M. N., and Bowden, W. B.: Profiles of temporal thaw depths beneath two arctic stream types using ground-penetrating radar, Permafrost and Periglacial Processes, 17, 341–355, 2006.

Carslaw, H. S. and Jaeger, J. C.: Conduction of Heat in Solids, Oxford University Press, Oxford, 2nd edn., 1959.

Couture, N. J. and Pollard, W. H.: Modelling geomorphic response to climatic change, Climatic Change, 85, 407–431, 2007.

Dallimore, S. R., Wolfe, S. A., and Solomon, S. M.: Influence of ground ice and permafrost on coastal evolution, Richards Island, Beaufort Sea coast, N.W.T., Canadian Journal of Earth Sciences, 33, 664–675, https://doi.org/10.1139/e96-050, 1996.

Davis, J. L., Scott, W. J., Morey, R. M., and Annan, A. P.: Impulse radar experiments on permafrost near Tuktoyaktuk, Northwest Territories, Canadian Journal of Earth Sciences, 13, 1584–1590, 1976.

De Pascale, G. P., Pollard, W. H., and Williams, K. K.: Geophysical mapping of ground ice using a combination of capacitive coupled resistivity and ground-penetrating radar, Northwest Territories, Canada, Journal of Geophysical Research: Earth Surface, 113, 2008.

Doolittle, J. A. and Nelson, F. E.: Characterising relict cryogenic macrostructures in mid-latitude areas of the USA with three-dimensional ground-penetrating radar, Permafrost and Periglacial Processes, 20, 257–268, https://doi.org/10.1002/ppp.644, 2009.

Edemsky, D. E., Tumskoy, V. E., and Prokopovich, I. V.: Ground penetrating radar survey of Arctic polygonal wedge structures, Russian Geology and Geophysics, 65, 767–778, https://doi.org/10.2113/RGG20234628, 2024.

Erkens, E., Angelopoulos, M., Tronicke, J., Dallimore, S. R., Whalen, D., Boike, J., and Overduin, P. P.: Mapping subsea permafrost around Tuktoyaktuk Island (Northwest Territories, Canada) using electrical resistivity tomography, The Cryosphere, 19, 997–1012, https://doi.org/10.5194/tc-19-997-2025, 2025.

Gacitúa, G., Uribe, J., Tamstorf, M. P., and Kristiansen, S. M.: Mapping of permafrost surface and active layer properties using GPR: a comparison of frequency dependencies, in: 2011 6th International Workshop on Advanced Ground Penetrating Radar (IWAGPR), pp. 1–5, IEEE, 2011.

Government of Canada: Tidal information – Tuktoyaktuk (06485), https://tides.gc.ca/en/stations/06485/, 2025.

Hansen, J., Ruedy, R., Sato, M., and Lo, K.: Global surface temperature change, Reviews of Geophysics, 48, RG4004, https://doi.org/10.1029/2010RG000345, 2010.

Hopky, G. E., Chiperzak, D. B., Lawrence, M. J., and de March, L.: Seasonal salinity, temperature and density data for Tuktoyaktuk Harbour and Mason Bay, NWT, 1980 to 1988, Canadian data report of fisheries and aquatic sciences, Department of Fisheries and Oceans, Canada, 1990.

https://doi.org/10.5194/egusphere-2026-5431
Preprint. Discussion started: 22 September 2026

Irrgang, A. M., Lantuit, H., Gordon, R. R., Piskor, A., and Manson, G. K.: Impacts of past and future coastal changes on the Yukon coast – threats for cultural sites, infrastructure, and travel routes, Arctic Science, 5, 107–126, https://doi.org/10.1139/as-2017-0041, 2019.

Khan, M. W., Martin, J., and Lim, M.: Instrumentation of low-cost IoT agnostic data capturing platform with enhanced sampling and bandwidth capabilities for subsurface characterization, IEEE Transactions on Instrumentation and Measurement, 2024.

Kokelj, S. V., Lantz, T. C., Solomon, S., Pisaric, M. F., Keith, D., Morse, P., Thienpont, J. R., Smol, J. P., and Esagok, D.: Using multiple sources of knowledge to investigate northern environmental change: regional ecological impacts of a storm surge in the outer Mackenzie Delta, NWT, Arctic, 65, 257–272, 2012.

Lapham, L. L., Dallimore, S. R., Magen, C., Henderson, L. C., Powers, L. C., Gonsior, M., Clark, B., Côté, M., Fraser, P., and Orcutt, B. N.: Microbial greenhouse gas dynamics associated with warming coastal permafrost, Western Canadian Arctic, Frontiers in Earth Science, 8, 582 103, https://doi.org/10.3389/feart.2020.582103, 2020.

Lenssen, N. J., Schmidt, G. A., Hansen, J. E., Menne, M. J., Persin, A., Ruedy, R., and Zyss, D.: Improvements in the GISTEMP uncertainty model, Journal of Geophysical Research: Atmospheres, 124, 6307–6326, https://doi.org/10.1029/2018JD029522, 2019.

Lewkowicz, A. G., O'Neill, H. B., Wolfe, S. A., Roy-Léveillée, P., Roujanski, V. E., Hoeve, E., Gruber, S., Brooks, H., Rudy, A. C. A., Koenig, C. E. M., Brown, N., and Bonnaventure, P. P.: Glossary of Permafrost Science and Engineering, Canadian Permafrost Association, https://doi.org/10.3138/cpa-gpse, 2025.

Lim, M., Whalen, D., Martin, J., Mann, P. J., Hayes, S., Fraser, P., Berry, H. B., and Ouellette, D.: Massive ice control on permafrost coast erosion and sensitivity, Geophysical Research Letters, 47, e2020GL087 917, 2020.

Lunardini, V.: Theory of n-factors and correlations of data, in: Proceedings of the Third International Conference on Permafrost, 10–13 July 1978, Edmonton, Alberta, Canada, vol. 1, p. 40, 1978.

Mackay, J. R.: The world of underground ice, Annals of the Association of American Geographers, 62, 1–22, 1972.

Manson, G. K. and Solomon, S. M.: Past and future forcing of Beaufort Sea coastal change, Atmosphere-Ocean, 45, 107–122, https://doi.org/10.3137/ao.450204, 2007.

Moorman, B. J., Robinson, S. D., and Burgess, M. M.: Imaging periglacial conditions with ground-penetrating radar, Permafrost and Periglacial Processes, 14, 319–329, 2003.

Munroe, J. S., Doolittle, J. A., Kanevskiy, M. Z., Hinkel, K. M., Nelson, F. E., Jones, B. M., Shur, Y., and Kimble, J. M.: Application of ground-penetrating radar imagery for three-dimensional visualisation of near-surface structures in ice-rich permafrost, Barrow, Alaska, Permafrost and Periglacial Processes, 18, 309–321, https://doi.org/10.1002/ppp.594, 2007.

Nakamura, Y.: A method for dynamic characteristics estimation of subsurface using microtremor on the ground surface, Quarterly Report of the Railway Technical Research Institute, 30, 25–33, 1989.

Overduin, P. P., Westermann, S., Yoshikawa, K., Haberlau, T., Romanovsky, V., and Wetterich, S.: Geoelectric observations of the degradation of nearshore submarine permafrost at Barrow (Alaskan Beaufort Sea), Journal of Geophysical Research: Earth Surface, 117, F02 004, https://doi.org/10.1029/2011JF002088, 2012.

Overduin, P. P., Haberland, C., Ryberg, T., Kneier, F., Jacobi, T., Grigoriev, M. N., and Ohrnberger, M.: Submarine permafrost depth from ambient seismic noise, Geophysical Research Letters, 42, 7581–7588, https://doi.org/10.1002/2015GL065409, 2015.

Overduin, P. P., Schneider von Deimling, T., Miesner, F., Grigoriev, M., Ruppel, C., Vasiliev, A., Lantuit, H., Juhls, B., and Westermann, S.: Submarine permafrost map in the Arctic modeled using 1-D transient heat flux (SuperMAP), Journal of Geophysical Research: Oceans, 124, 3490–3507, https://doi.org/10.1029/2018JC014675, 2019.

https://doi.org/10.5194/egusphere-2026-5431
Preprint. Discussion started: 22 September 2026

Ramage, J., Jungsberg, L., Wang, S., Westermann, S., Lantuit, H., and Heleniak, T.: Population living on permafrost in the Arctic, Population and Environment, 43, 22–38, https://doi.org/10.1007/s11111-020-00370-6, 2021.

Rantanen, M., Karpechko, A. Y., Lipponen, A., Nordling, K., Hyvärinen, O., Ruosteenoja, K., Vihma, T., and Laaksonen, A.: The Arctic has warmed nearly four times faster than the globe since 1979, Communications Earth & Environment, 3, 168, https://doi.org/10.1038/s43247-022-00498-3, 2022.

Schennen, S., Tronicke, J., Wetterich, S., Allroggen, N., Schwamborn, G., and Schirrmeister, L.: 3D ground-penetrating radar imaging of ice complex deposits in northern East Siberia, Geophysics, 81, WA195–WA202, https://doi.org/10.1190/geo2015-0129.1, 2016.

Schennen, S., Wetterich, S., Schirrmeister, L., Schwamborn, G., and Tronicke, J.: Seasonal impact on 3D GPR performance for surveying Yedoma ice complex deposits, Frontiers in Earth Science, 10, 741 524, https://doi.org/10.3389/feart.2022.741524, 2022.

Schuur, E. A. G., McGuire, A. D., Schädel, C., Grosse, G., Harden, J. W., Hayes, D. J., Hugelius, G., Koven, C. D., Kuhry, P., Lawrence, D. M., Natali, S. M., Olefeldt, D., Romanovsky, V. E., Schaefer, K., Turetsky, M. R., Treat, C. C., and Vonk, J. E.: Climate change and the permafrost carbon feedback, Nature, 520, 171–179, https://doi.org/10.1038/nature14338, 2015.

Shen, Y., Zuo, R., Liu, J., Tian, Y., and Wang, Q.: Characterization and evaluation of permafrost thawing using GPR attributes in the Qinghai-Tibet Plateau, Cold Regions Science and Technology, 151, 302–313, 2018.

Stefan, J.: Über die Theorie der Eisbildung, insbesondere über die Eisbildung im Polarmeere, Annalen der Physik, 278, 269–286, 1891.

Sudakova, M., Sadurtdinov, M., Skvortsov, A., Tsarev, A., Malkova, G., Molokitina, N., and Romanovsky, V.: Using ground penetrating radar for permafrost monitoring from 2015–2017 at CALM sites in the Pechora river delta, Remote Sensing, 13, 3271, 2021.

Watanabe, T., Matsuoka, N., and Christiansen, H. H.: Ice- and soil-wedge dynamics in the Kapp Linné area, Svalbard, investigated by two- and three-dimensional GPR and ground thermal and acceleration regimes, Permafrost and Periglacial Processes, 24, 39–55, https://doi.org/10.1002/ppp.1767, 2013.

Whalen, D., Forbes, D. L., Kostylev, V. E., Lim, M., Fraser, P., Nedimović, M. R., and Stuckey, S.: Mechanisms, volumetric assessment, and prognosis for rapid coastal erosion of Tuktoyaktuk Island, an important natural barrier for the harbour and community, Canadian Journal of Earth Sciences, 59, 945–960, https://doi.org/10.1139/cjes-2021-0101, 2022.

Williams, P. J. and Smith, M. W.: The Frozen Earth: Fundamentals of Geocryology, Studies in Polar Research, Cambridge University Press, Cambridge, 1991.